Acta Pharmaceutica Sinica B 2026;16(5):3109−3127

Chinese Pharmaceutical Association
Institute of Materia Medica, Chinese Academy of Medical Sciences

Acta Pharmaceutica Sinica B

www.elsevier.com/locate/apsb
www.sciencedirect.com

ORIGINAL ARTICLE

A new approach to discovering a broad-spectrum anti-respiratory virus drug: Tubeimoside II modulates host factor PACT to potentiate the RIG-I antiviral pathway

Xian Liu[a,†], Dan Xie[a,†], Mengyao Cui[a], Shuran Li[a], Xiaowei Yang[a], Juan Zhang[b], Yu Zhang[a], Shan Cao[a], Lei Bao[a], Zihan Geng[a], Jing Sun[a], Ronghua Zhao[a], Shuangrong Gao[a], Xiaolan Cui[a], Chengpeng Sun[b,*], Shanshan Guo[a,*]

[a]*State Key Laboratory for Quality Ensurance and Sustainable Use of Dao-di Herbs, Institute of Chinese Materia Medica, China Academy of Chinese Medical Sciences, Beijing 100700, China*
[b]*School of Chinese Materia Medica, School of Medical Technology, Tianjin Key Laboratory of Therapeutic Substance of Traditional Chinese Medicine, Tianjin University of Traditional Chinese Medicine, Tianjin 301617, China*

Received 10 May 2025; received in revised form 16 January 2026; accepted 18 January 2026

KEY WORDS

PACT;
Host factor;
Respiratory viruses;
Ligand compounds;
Tubeimoside II;
Antiviral;
RIG-I signaling pathway;
Broad-spectrum

Abstract PACT (PKR activating protein)/PRKRA is a quintessential double-stranded RNA (dsRNA) binding protein that has recently surfaced as a novel and compelling antiviral target, exhibiting resistance against a spectrum of respiratory viruses. Despite this, no antiviral ligand compounds targeting PACT have been identified to date. In this study, we conducted an extensive screening within natural products, leading to the development of an exceptional PACT-T78 site ligand, tubeimoside II (TBM II). TBM II effectively combats a spectrum of respiratory viruses, including the coronaviruses HCoV-OC43 and SARS-CoV-2, as well as the influenza A H1N1 virus (IAV-H1N1), by reducing viral loads and inhibiting viral replication and proliferation both *in vitro* and *in vivo*. Single-cell RNA sequencing demonstrated that TBM II significantly impacts the RIG-I signaling pathway associated with PACT. We found that when PACT was knocked down or when RIG-I, MAVS, or IFN-β were knocked out, the ability of TBM II to activate the RIG-I signaling pathway was diminished, resulting in a corresponding attenuation of its

*Corresponding authors.
E-mail addresses: suncp146@163.com (Chengpeng Sun), ssguo@icmm.ac.cn (Shanshan Guo).
[†]These authors made equal contributions to this work.

Peer review under the responsibility of Chinese Pharmaceutical Association and Institute of Materia Medica, Chinese Academy of Medical Sciences.

https://doi.org/10.1016/j.apsb.2026.03.020

antiviral efficacy. These findings indicated that TBM II targets PACT to activate the RIG-I signaling pathway, thereby increasing the secretion of type I interferon IFN-β, ultimately promoting the innate immune response and achieving antiviral efficacy. In summary, our work identified TBM II as a new generation PACT ligand that activating the RIG-I signaling pathway, achieving broad-spectrum antiviral effects.

1. Introduction

Acute respiratory viruses, spanning influenza A/B, coronaviruses, and adenovirus serotypes, constitute primary etiological agents for heterogeneous respiratory tract pathologies. These viruses are characterized by rapid onset, high infectivity, swift transmission, and high mortality rates, which frequently trigger seasonal outbreaks and global pandemics[1]. Moreover, the relentless emergence of SARS-CoV-2 variants has caused a regression in global life expectancy by nearly a decade[2]. The current majority of antiviral drugs for respiratory viruses target specific viruses, such as oseltamivir for influenza. And the growing problem of antiviral resistance, further constraints therapeutic outcomes. Therefore, the development of broad-spectrum and highly effective antiviral drugs remains a major challenge[3]. Host-targeted antiviral (HTA) strategies have garnered significant attention in recent years[4]. Inhibitors targeting host factors such as DHODH demonstrated potent efficacy against diverse RNA viruses, including SARS-CoV-2 and influenza viruses, exhibiting broad-spectrum antiviral activity[5]. Due to the high dependence of viruses on host cellular mechanisms during replication, drugs targeting host factors can disrupt the life cycles of multiple virus types, thereby exhibiting broad-spectrum activity[6]. Secondly, compared to drugs that directly target viral proteins, HTA drugs are less prone to resistance development, as they act on host factors essential for viral replication, which are often shared by different viruses. Moreover, HTA drugs development offers rapid-response capability during emerging viral outbreaks, as evidenced during the COVID-19 pandemic where HTAs provided critical therapeutic countermeasures against novel pathogens[7,8]. Hence one can see that Host-targeted antiviral approaches offer an evolutionary leap in drug design, overcoming limitations imposed by viral mutation bottlenecks.

PKR activating protein (PACT), a critical regulator of the PKR kinase in interferon signaling, modulates viral replication dynamics and host immunoregulatory mechanisms[9]. PACT has emerged as a critical factor in the intricate interplay between host cells and invading viruses, representing a potential host target for exerting antiviral activity[10,11]. Once a virus invades the host cell, it can rapidly sense viral dsRNA through PACT, subsequently acting on the cytoplasmic RNA virus receptors RIG-I/MDA5[12]. RIG-I functions as a cytoplasmic RNA sensor, mediating antiviral/anti-tumor immunity *via* CTD-dependent viral dsRNA recognition and CARD-triggered MAVS-IRF3/7 signaling to induce type I interferon (IFN-I) production[13]. Consequently, activating the PACT/RIG-I axis not only augments host antiviral defenses but also supports potential targets for developing next-generation broad-spectrum antivirals.

It is worth noting that traditional Chinese medicine compounds (TCM compounds) hold unique advantages as antiviral agents by targeting host factors[14−17]. Their multi-target mechanisms enable simultaneous intervention at multiple stages of the viral life cycle, including inhibiting viral entry into host cells and blocking viral replication and release[18−21]. This multidimensional approach not only improves antiviral efficacy but also reduces the risk of viral drug resistance. Tubeimoside II (TBM II), a naturally occurring triterpenoid saponin compound derived from traditional Chinese medicine, possesses a well-established research foundation in oncology and inflammation[22]. However, the antiviral properties of TBM II were known limited. To our knowledge, only two recent studies have reported that TBM II displays antiviral effect on human immunodeficiency virus (HIV)[23] and SARS-CoV-2[24]. In this study, we first demonstrated that TBM II also displayed broad-spectrum antiviral activity against coronaviruses (SARS-CoV-2, HCoV-OC43) and influenza virus (IAV-H1N1 FM1) *in vitro*, which were consistent with the SARS-CoV-2 inhibition reported previously[24]. A key finding is that TBM II demonstrates therapeutic efficacy against HCoV-OC43 and IAV-H1N1 infections in mice, which has not been previously reported. Furthermore, we found that TBM II binds to PACT, with the binding site likely located at the PACT-T78 site. This represents the first reported ligand discovery targeting PACT to date. We proved that TBM II targets PACT to promote the RIG-I signaling pathway, thereby increasing the secretion of IFN-I and enhancing the antiviral innate immunity to achieve antiviral effects. Therefore, we proposed that TBM II, as a ligand compound, unleashes its broad-spectrum antiviral potential when acting on the robust antiviral host target PACT. Our finding lays a valuable foundation for the future exploration of antiviral drugs based on this target.

2. Results

2.1. The high-throughput screening identifies TCM compounds targeting PACT

Firstly, we employed a virtual screening approach to identify promising TCM compounds. Ten high-affinity compounds exhibiting binding energies of −7 to −9 kcal/mol were screened: punicalagin (PUN), tubeimoside III (TBM III), tubeimoside II (TBM II), prosapogenin A (Progenin III), theaflavin-3′-Gallate (TF-2B), tubeimoside I (TBM I), chebulagic acid (CA), geraniin (GER), hypericum (HY), and ophiopogonin-D (OPD) (Supporting Information Fig. S1A and Table S1). Subsequently, we selected the top eight compounds based on their binding affinity for further validation of their antiviral activity against the transcription and replication-competent SARS-CoV-2 virus-like-particles (trVLP). This trVLP expresses a reporter gene (GFP) replacing viral nucleocapsid gene (N), which is required for viral genome packaging and virion assembly (SARS-CoV-2 GFP/ΔN trVLP). And it can be detected and visualized as green fluorescence (GFP) under

a high-content imaging system to assess the viral infection, thereby determining whether the tested compounds exhibit activity against SARS-CoV-2 (Fig. 1A). We observed that the positive control drug, Azvudine (FNC), significantly inhibited the proliferation and spread of SARS-CoV-2. Among the eight tested compounds, all exhibited varying degrees of antiviral activity. Notably, TBM II demonstrated significant antiviral effects across all three dosages, with its efficacy most closely resembling that of FNC and exhibiting a strong affinity for PACT (Fig. 1B and Fig. S1B). To determine the antiviral efficacy of TBM II, we measured the viral loads of coronavirus SARS-CoV-2, HCoV-OC43, and influenza virus IAV-H1N1/FM1 in different cell types following treatment with TBM II after viral infection. These results indicated that TBM II exhibits antiviral activity against all

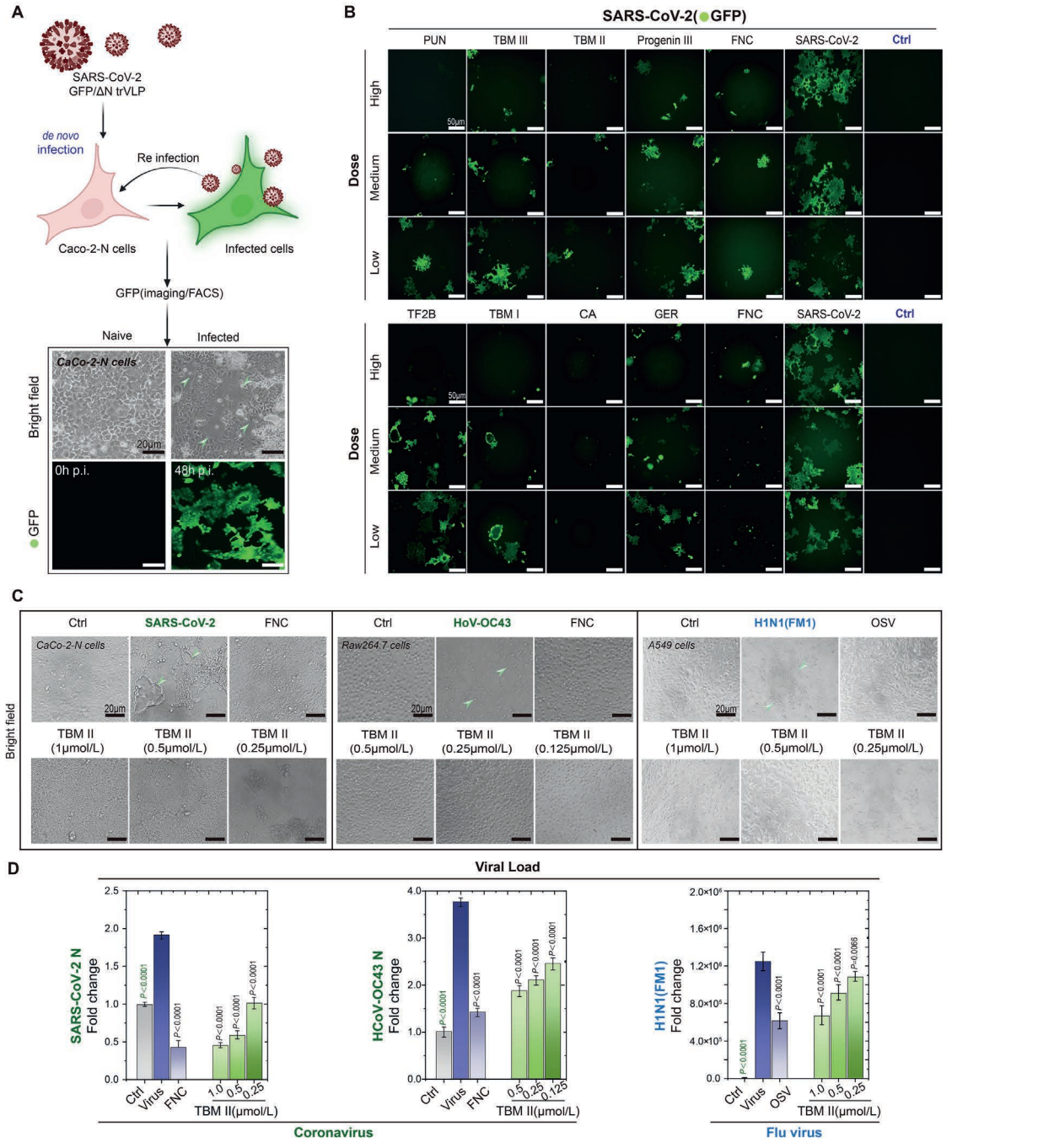

Figure 1 TBM II exerts antiviral activity against respiratory viruses *in vitro*. (A) The characteristic feature of SARS-CoV-2 GFP/ΔN trVLP infection in Caco-2-N cells is the enhancement of GFP fluorescence signal. (B) The intensity of green fluorescent protein (GFP) signal following viral infection and subsequent administration of eight compounds. (C) TBM II alleviates cytopathic effects induced by the three viruses. (D) TBM II reduces the viral load in Caco-2-N, Raw, and A549 cells following infection with the three viruses ($n=3$). Scale bar = 50 μm/20 μm. Data present as Mean ± SD, H-high dose, M-medium dose, L-low dose. *P*-value is generated by comparing between the following groups: Ctrl *vs* Virus (green); Virus *vs* FNC/OSV/different dosages of TBM II (black). All experimental groups, except the Ctrl group, were infected with the virus.

three viruses (Fig. 1C and D), and it also exerts a potent inhibitory effect on the spread of the GFP fluorescence signal of the SARS-CoV-2 GFP/ΔN trVLP (Fig. S1C). Moreover, we evaluated the antiviral efficacy of TBM II against SARS-CoV-2 in a biosafety level 3 (BSL-3) laboratory and observed that TBM II treatment significantly reduced viral titers in Calu-3 cells (Fig. S1D). These results suggested that TBM II possess broad-spectrum antiviral activity against respiratory viruses. Therefore, TBM II was designated as the primary compound for this study to investigate whether its antiviral effects were mediated through PACT.

2.2. TBM II exhibits high-affinity binding to PACT

To confirm whether PACT serves as a target for TBM II, we applied TBM II-mediated pull-down experiments for target identification by using TBM II-bead complex (Fig. 2A). In TBM II-mediated pull-down experiment showed that TBM II bind to PACT, which was supported by results from drug affinity responsive target stability (DARTS) experiment (Fig. 2B). Meanwhile, TBM II-mediated pull-down experiment also indicated a distinct protein band appeared at approximately 34 kDa through silver staining. According to LC−MS/MS analysis, this protein band was identified as PACT and was further validated by Western blotting (Fig. 2C and Supporting Information Fig. S2A). Cellular thermal shift analysis (CETSA) showed that the apparent melting curve of PACT shifted significantly to the right following TBM II treatment, corresponding to an increased Tm of 53.75 °C, which demonstrates enhanced protein stability (Fig. 2D). PACT protein exhibited a dose-dependent reduction in thermal stability upon TBM treatment (Fig. 2E), and the dissociation rate constant of 5.37 μmol/L were yielded by surface plasmon resonance (SPR) experiments (Fig. 2F). These results showed that TBM II mediated stabilization of PACT. Furthermore, we employed molecular docking to identify Thr78 of PACT as the binding site for TBM II and PACT (Fig. 2G). In order to confirm the role of this amino acid residue, Thr78 was mutated into Ala (Thr78Ala). Microscale thermophoresis (MST) results suggested that Thr78Ala mutation impaired the affinity of TBM II and PACT because their K_d value was decreased to 133.1 μmol/L (Fig. 2H). Meanwhile, Thr78Ala mutation abolished the binding and the pro-stability of TBM II toward PACT in the experiments of pull-down, CETSA, and DARTS (Fig. S2B), which suggested that Thr78 displayed a critical role in the binding of TBM II with PACT.

2.3. TBM II mediates antiviral protection against respiratory viruses in vivo

After conducting *in vitro* pharmacodynamic evaluations, we accessed the therapeutic efficacy of TBM II in virally infected mice. ICR and BALB/c mice received intranasal inoculations of IAV-H1N1/FM1 and HCoV-OC43, respectively, and TBM II treatment was initiated concurrently, with administration sustained for 5 days (Fig. 3A). The dosages were as follows: TBM II H (high) = 2.6 mg/kg, M (medium) = 1.3 mg/kg, and L (low) = 0.65 mg/kg; FNC (2.0 mg/kg); OSV (27.5 mg/kg). Micro-CT imaging on day 5 post-treatment revealed that significant pulmonary volume expansion and focal ground-glass opacities in the lungs of virus-infected mice, while TBM II treatment substantially mitigated these pathological manifestations (Figs. 3B and C, and Supporting Information Fig. S3). Additionally, we evaluated antiviral efficacy by quantifying pulmonary viral loads in mouse lung tissues using RT-qPCR. The result showed that TBM II treatment significantly reduced the viral load, confirming dose-dependent inhibition of viral replication and pulmonary dissemination (Fig. 3D). Subsequent immunophenotyping of murine whole blood by multiparametric flow cytometry quantified the dynamics of CD4+/CD8+ co-expression across T-lymphocyte subsets. We observed that TBM II treatment restored the down-regulation of both $CD4^+$ and $CD8^+$ expression caused by viral infection with differential efficacy (Figs. 3E−H). These findings support a preliminary model whereby TBM II provides antiviral protection primarily through host immune enhancement.

2.4. TBM II alleviates pulmonary inflammation induced by respiratory viruses

Respiratory viral infections commonly induce pulmonary inflammation. Upon dissection, influenza-infected murine lungs exhibited polymorphic erythematous mottled lesions (Figs. 4A and B). Histological examination *via* H&E staining of pulmonary lobes revealed mild-to-moderate alveolar wall thickening, interstitial congestion, and edema in both IAV-H1N1/FM1 and HCoV-OC43 infection models. These lesions were accompanied by marked neutrophilic, lymphocytic, and mononuclear macrophage infiltration, as well as intra-alveolar inflammatory exudates (Figs. 4C and D). The bronchiolar epithelial cells exhibited mild to moderate swelling, with some undergoing degeneration, necrosis, and desquamation, leading to a significantly increased lung index. Administration of TBM II significantly alleviated these pathological changes and reduced the lung index (Figs. 4E and F). To further investigate the inflammatory response, we utilized Luminex liquid-phase chip analysis to measure inflammatory cytokine expression in mice lung tissues. The results revealed that the levels of TNF-α, IL-1β, IL-6, and IFN-γ were markedly elevated in mouse lungs following infection with IAV-H1N1/FM1 and HCoV-OC43 virus. Administration of TBM II resulted in a significant decrease in these inflammatory cytokines, demonstrating its ability to mitigate pulmonary inflammation caused by respiratory viral infections such as HCoV-OC43 and IAV-H1N1/FM1 virus (Figs. 4G and H). Given evidence that HCoV-OC43 infection can invade the brain and induce neuropathological alterations[25,26], we performed H&E and Nissl staining on mice brain sections to evaluate histopathological changes and concurrently quantified viral load in brain tissues. Neuropathological analysis revealed loosened interstitial architecture and shrunken neurons with hyperchromatic staining, ill-defined nucleocytoplasmic boundaries, and sporadic neuronophagia in cortical/hippocampal regions post-infection (Supporting Information Figs. S4A and S4B). The viral load in brain tissues also increased significantly, mirroring pulmonary levels. Administration of TBM II substantially attenuated viral load and ameliorated neuropathological alterations (Fig. S4C). These results indicated that TBM II not only exerts antiviral effects in the lungs but also demonstrates antiviral and anti-inflammatory effects in the brain.

2.5. TBM II primarily affects the gene expression of macrophages and epithelial cells in the lung following influenza virus infection

To determine whether the host target PACT is influenced by viral infections *in vivo*, we infected ICR mice with IAV-H1N1/FM1 virus and administered TBM II (2.6 mg/kg). Utilizing single-cell RNA sequencing (scRNA-seq), we first characterized the

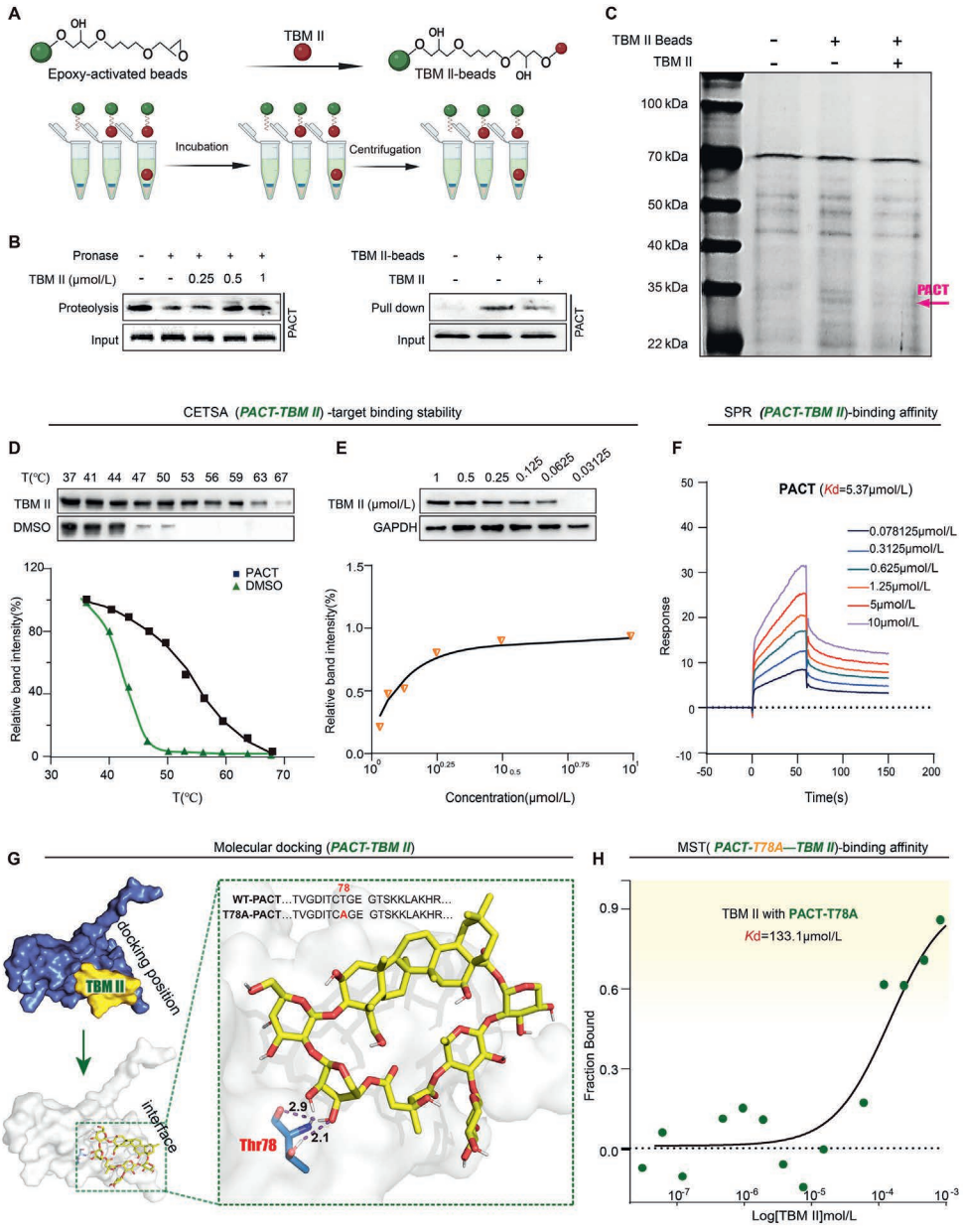

Figure 2 TBM II exhibits stable binding to the target PACT. (A) Epoxy-activated beads were conjugated with TBM II to fabricate the TBM II-bead complex. (B) The binding of TBM II to PACT was validated using the DARTS assay. (C) Target protein capture assays confirmed PACT as the target protein of TBM II. (D) The trend of target protein solubility following the administration of TBM II, as detected by CETSA, in relation to temperature changes. (E) The isothermal dose-response curve following CETSA upon administration of TBM II. (F) The determination of the binding affinity strength between TBM II and PACT using the dissociation rate constant (K_d) obtained from SPR detection. (G) Molecular docking revealed Thr78 of PACT as the key binding residue for TBM II. (H) MST confirmed reduced binding affinity between TBM II and Thr78Ala-mutated PACT.

pulmonary cell types. The results indicated that a total of 13 distinct cell types, designated as cells B cells, Endothelial cells, Macrophages, Smooth muscle cells, Basophils, Epithelial cells, Monocytes, T cells, DCs, Fibroblast, Neutrophils, and NK, an additional category of unknown cells in lung tissues (Figs. 5A−C, and Supporting Information Fig. S5A). By aligning key viral genes (NEP/NS1-CY087788.1, NP-CY087787.1, PB1-CY087790.1, PB2-CY087791.1) with other relevant viral gene sequences, we identified that the virus predominantly localizes to macrophages and epithelial cells in lungs following infection, with the two cell types characterized by maker gene expression of *Krt18 and Krt8* for epithelial cells, and *Cd68*, *Csf1r*, and *C1qb* for macrophages (Fig. 5D and Fig. S5B). We compared the gene expression profiles between the control group and the infection group, as well as between the infection group and the TBM II-treated group. The results showed that the number of

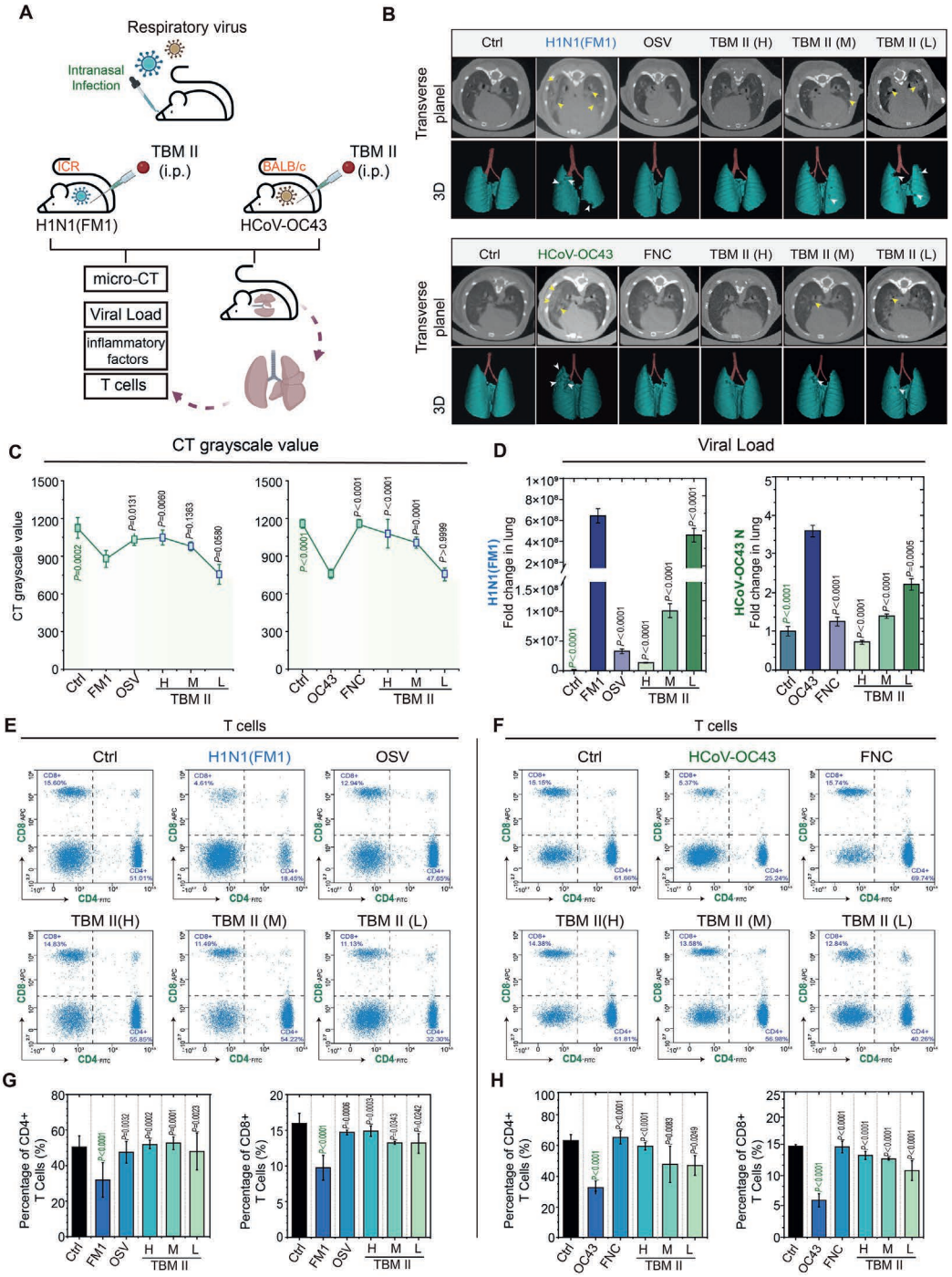

Figure 3 TBM II exerts antiviral activity against respiratory viruses *in vivo*. (A) Pharmacodynamic study design in virus-infected mice. (B) Micro-CT showing TBM II-mediated mitigation of pulmonary lesions in IAV-H1N1/FM1-and HCoV-OC43-infected mice. (C) Lung gray-scale values by micro-CT ($n=4$). (D) TBM II reduced viral load in lungs by RT-qPCR ($n=4$). (E, F) FACS representative graph of $CD4^+$ and $CD8^+$ T cells in the mouse plasma. (G, H) TBM II elevated the levels of $CD4^+$ and $CD8^+$ T cells in the mouse plasma ($n=6$). Data present as mean ± SD, *P*-value is generated by comparing between the following groups: Control *vs* Two viral infection models (green); Two viral infection models v*s* FNC/OSV/different dosages of TBM II (black). All experimental groups, except the Ctrl group, were infected with the virus.

differentially expressed genes was higher in macrophages and epithelial cells, suggesting that TBM II primarily affects the gene expression of these two cell populations in the lung tissues of mice following influenza virus infection (Figs. 5E−G, and Fig. S5C).

2.6. TBM II is intimately linked to the PACT and RIG-I signaling axis

Subsequently, we performed comparative enrichment analysis on cells derived from lung tissues of virus-infected and normal mice.

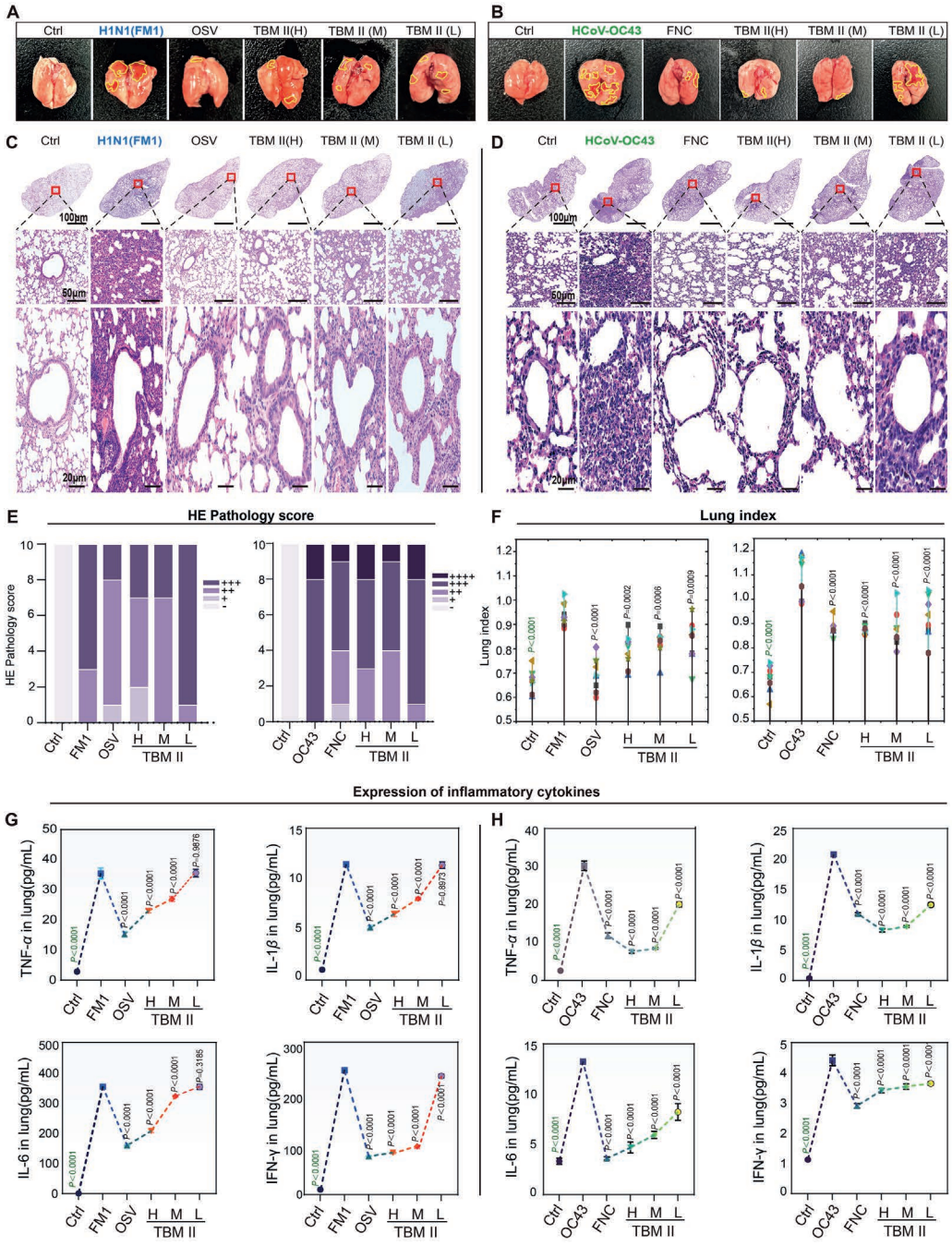

Figure 4 TBM II alleviates lung inflammation caused by respiratory viruses. (A, B) The condition of lung tissue damage in fresh lung samples following viral infection and administration of TBM II. (C, D) Microscopic examination of the H&E-stained sections of the left lung lobe tissue. (E) Histopathological scoring of H&E staining ($n=8$). (F) The impact of TBM II on lung index following infection with the two viruses ($n=8$). (G, H) The Luminex assay kit was used to detect the expression of inflammatory cytokines TNF-α, IL-1β, IL-6, and IFN-γ in lung tissues after infection with the two viruses and administration of TBM II ($n=6$). Scale bar = 20 μm/50 μm/100 μm. Data present as mean ± SD, *P*-value is generated by comparing between the following groups: Ctrl *vs* Two viral infection models (green); Two viral infection models *vs* FNC/OSV/different dosages of TBM II (black). All experimental groups, except the Ctrl group, were infected with the virus.

We observed that the pro-inflammatory cytokines IL-1β and IL-6 were up-regulated, while IL-10 was down-regulated, indicating that viral infection induced inflammation in pulmonary cells. Upon comparing whole-cell populations as well as epithelial and macrophage cells from the tissues of three groups of samples, we found that significant differences in expression levels of the genes related to Prkra and RIG-I signaling pathway related genes, including Rigi, Mavs, Irf3 and Irf7 (Fig. 6C and Supporting Information Fig. S6A). These results demonstrate a causal link between TBM II's antiviral efficacy and its modulation of the

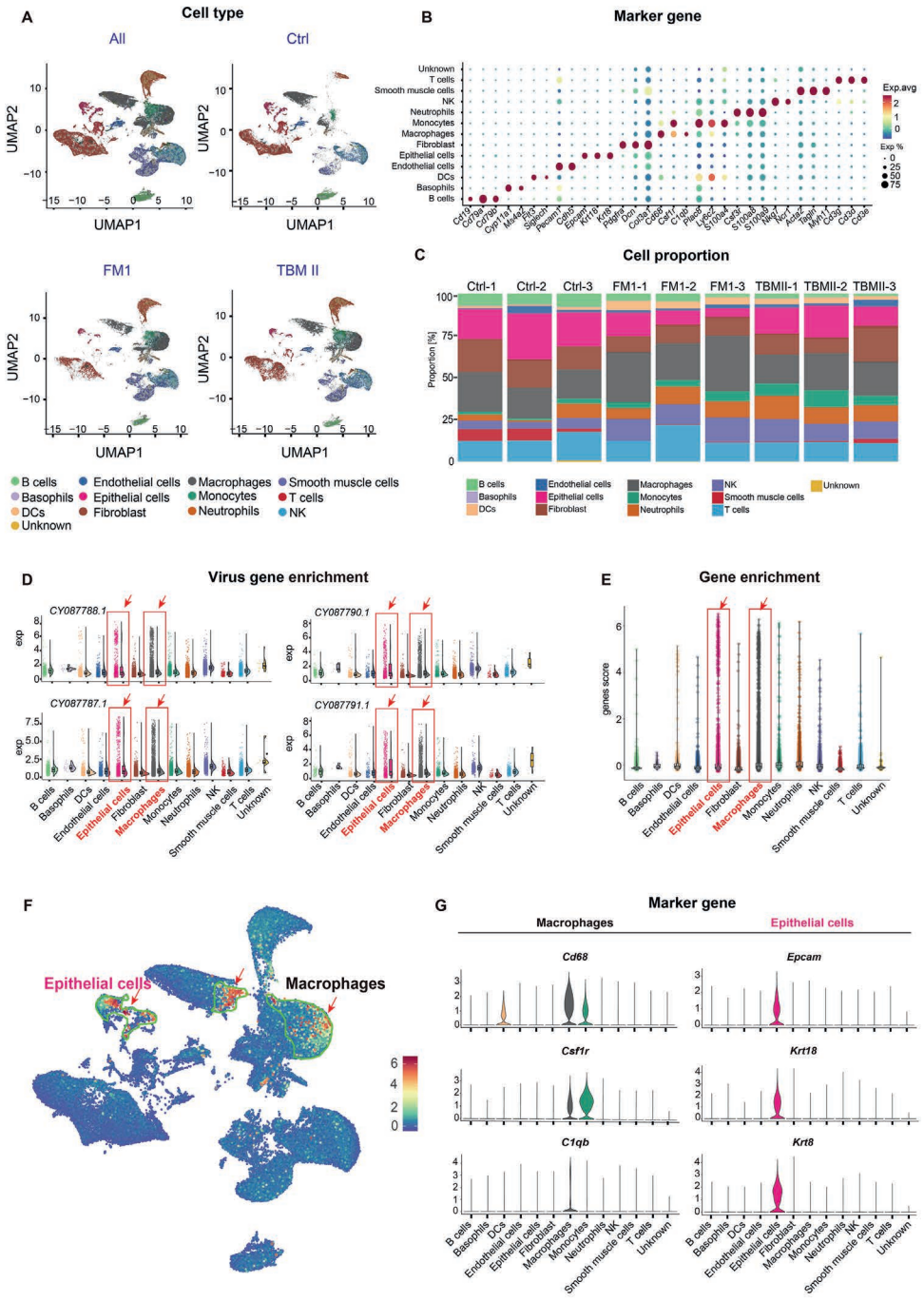

Figure 5 The cellular and gene distribution in the lungs of mice following viral infection. (A) UMAP visualization of 13 distinct cell clusters in lung of mice. (B) Marker gene annotation for each cluster. (C) Cell proportion diagrams for each sample group. (D) Cell type-specific expression of influenza virus genes (NEP/NS1: CY087788.1; NP: CY087787.1; PB1: CY087790.1; PB2: CY087791.1). (E, F) The enrichment degree of differentially expressed genes in 13 types of cells. (G) Violin plots depicting macrophage/epithelial cell gene signatures.

RIG-I-mediated signaling pathway. In addition, the scRNA-seq analysis indicated that viral infection attenuates the type I interferon signaling pathway and RIG-I-mediated signaling cascades (Fig. 6A and B). We therefore performed a dynamic time-course analysis in mice infected with influenza virus. The results revealed a progressive increase in viral load from Day 1 to Day 5 post-infection. However, key innate immune mediators, including PACT, RIG-I, and IFN-β, exhibited a biphasic expression pattern characterized by an initial upregulation followed by a subsequent downregulation (Figs. 7A and B, and Supporting Information Fig. S7A). These indicates that while viral infection initially triggers host innate immunity as a defense mechanism, viral proteins likely suppress the expression of these factors at later stages, a finding consistent with the work of Yi et al. [27]. Consequently, rescuing immune function during the later phase represents a viable therapeutic strategy to curb persistent viral

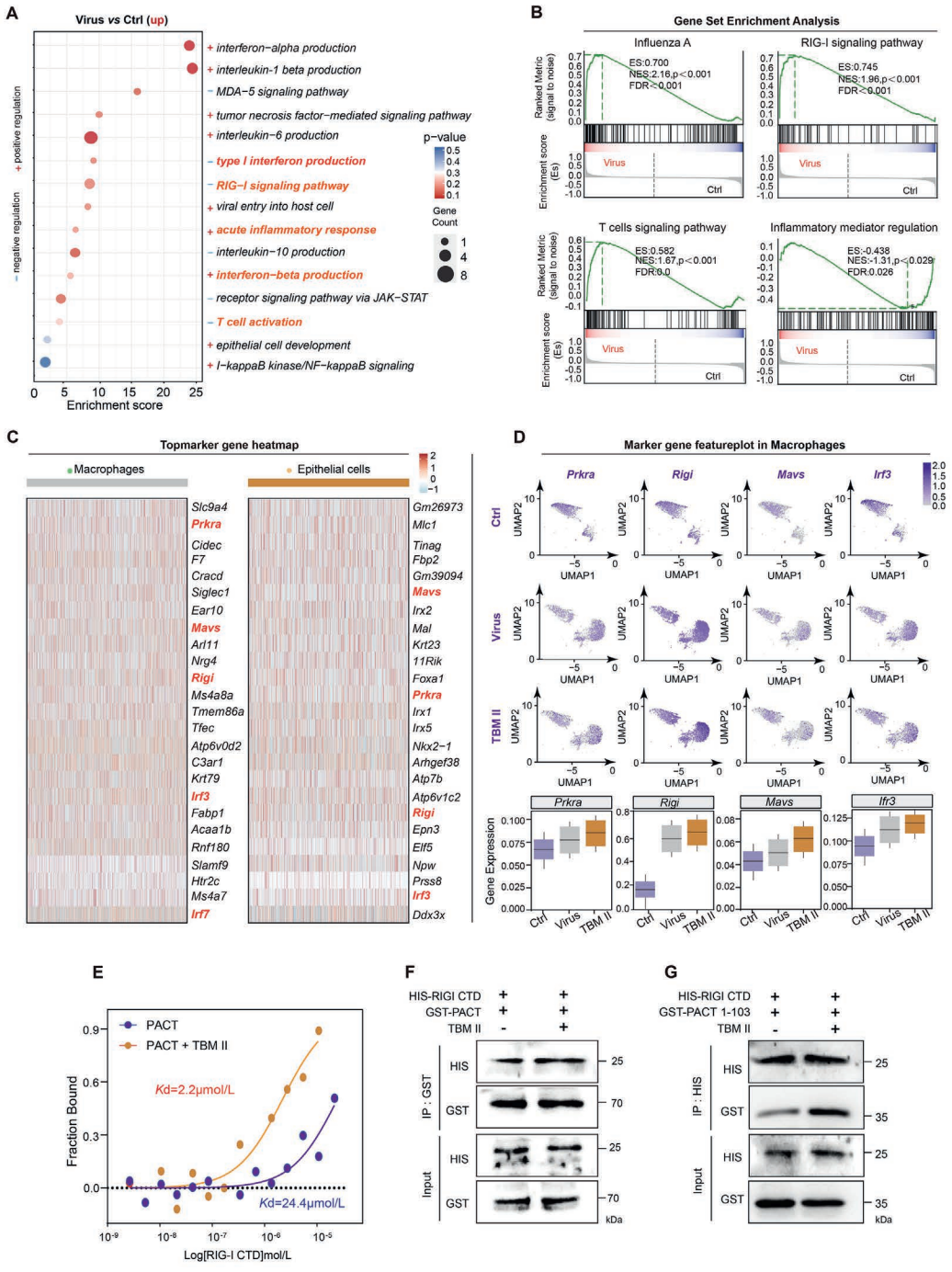

Figure 6 Single-Cell RNA Sequencing confirmed the relationship between TBM II and the PACT and RIG-I signaling pathways. (A) Cluster-specific pathway enrichment analysis of differentially expressed genes. (B) Gene Set Enrichment Analysis (GSEA) of the Dynamic Transcriptome in Response to IAV/H1N1/FM1 Infection. (C) The heatmap illustrates the top marker genes in Macrophages and epithelial cells. (D) The expression levels of PACT, RIG-I MAVS and IRF3 genes in macrophages following IAV/H1N1/FM1 virus infection and administration of TBM II. (E−G) Microscale thermophoresis (MST) analysis was employed to characterize TBM II's molecular interaction specificity with the C-terminal domains (CTD) of RIG-I and the 1-313 segment of PACT protein under *in vitro* conditions.

replication and mitigate virus-induced pathology. Upon analysis, we found that TBM II concurrently elevated the expression of Prkra, Rigi, Mavs, and Irf3 in pulmonary macrophages and epithelial cells (Fig. 6D and Fig. S6D), while suppressing a panel of pro-inflammatory genes, including *Stat4*, *Cd180*, *Pdcd4*, *Ifng*, *Prkcq*, *Aif1*, *Ccl4*, *Ccl5*, *Ccr5*, and *Xcl1* (Fig. S6B). Therefore, we propose a hypothesis that TBM II may target PACT to promote the binding of PACT and RIG-I, thereby activating the RIG-I signaling pathway, stimulating the production of IFN-I, and enhancing the antiviral innate immune response against viral

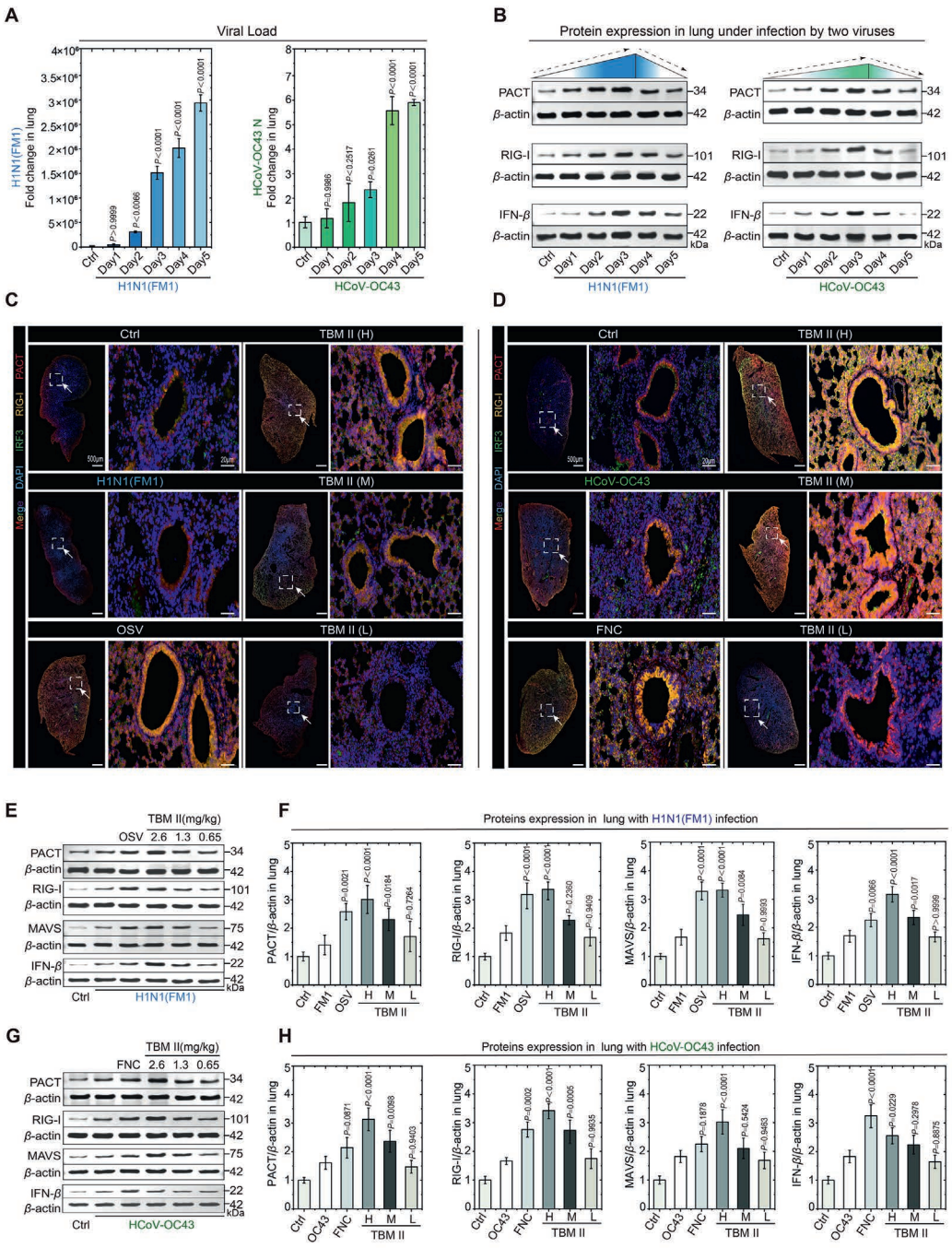

Figure 7 TBM II modulates PACT/RIG-I axis in infected lungs. (A) Dynamics of viral load in the lungs of mice after two viral infections from Day 1 to Day 5 after infection. (B) Western blot analysis of PACT, RIG-I, and IFN-β expression in lung from Day 1 to Day 5 post infection with two viruses ($n=4$). (C, D) Immunofluorescence images display the expression of PACT, RIG-I, and IRF-3 in mouse lung tissues following infection with two types of viruses and administration of TBM II (PACT→ red; RIG-I→ gold; IRF3→green) ($n=3$). (E–H) Western blot analysis reveals the alterations in protein levels of PACT, RIG-I, MAVS and IFN-β in mouse lung tissues subsequent to infection with two types of viruses and administration of TBM II ($n=4$). Scale bar = 500 μm/20 μm. Data present as mean ± SD, *P*-value is generated by comparing between the following groups: Control *vs* Two viral infection models in A; Two viral infection models *vs* FNC/OSV/different dosages of TBM II in F and H. All experimental groups, except the Ctrl group, were infected with the virus.

infections. To verify this hypothesis, we employed microscale thermophoresis (MST) and co-immunoprecipitation (Co-IP) assays to investigate the impact of TBM II on the interaction between PACT and RIG-I. The results indicated that TBM II not only affects the interaction between PACT and RIG-I but also enhances their binding, with the primary binding regions located

in the CTD domain of RIG-I and the 1-103 segment of the PACT protein (Figs. 6E−G and Fig. S6C). Given that alterations in the RIG-I signaling pathway can lead to changes in downstream immune responses, we next explored whether TBM II can modulate the RIG-I signaling pathway *in vitro* and *in vivo* through PACT to regulate the secretion of IFN-β.

2.7. TBM II modulates the immune response in mice following infection with IAV and HCoV-OC43 via the RIG-I signaling pathway

To validate the reliability of the scRNA-seq results, we performed immunofluorescence (IF) staining on lung tissue sections from mice continuously administered TBM II for 5 days post-infection with both viruses. The staining was carried out using fluorophore-conjugated antibodies specific for PACT, RIG-I, and IRF3. The results demonstrated that TBM II treatment enhanced the fluorescence intensity of all three proteins (Figs. 7C, D and Figs. S7C and D). We then assessed the regulatory effect of TBM II on downstream targets of the RIG-I signaling pathway, a key antiviral cascade. We observed that TBM II significantly elevated the protein expression levels of PACT, RIG-I, MAVS, and IFN-β in lung tissue following infection with both respiratory viruses. The positive drugs OSV and FNC also showed statistically significant effects equivalent to TBM II. However, OSV's impact on MAVS and FNC's effect on IRF3 phosphorylation levels were minor with no significant differences. Additionally, TBM II treatment mildly enhanced the phosphorylation level of IRF3, although a statistically significant increase was observed only at the high dose (Figs. 7E−H and Fig. S7B). Our data demonstrated that TBM II counteracts this immune evasion by up-regulating key RIG-I pathway components, thereby rescuing type I interferon secretion. Concordantly, transcriptional profiling of pulmonary tissue confirmed concomitant elevation of *Rigi* and *Ifnb1* mRNA abundance (Figs. S7E and F). These findings align with the single-cell transcriptomics data (Section 2.6), demonstrating TBM II-mediated potentiation of the RIG-I→MAVS→IRF3 signaling axis. This licensing cascade culminates in robust type I interferon (IFN-I) production and enhanced host antiviral defense programs.

2.8. PACT is a determinant of the in vitro antiviral efficacy of TBM II

To determine whether TBM II exerts its antiviral effects by targeting PACT and whether it affects the RIG-I signaling pathway, we performed PACT knockdown or overexpression experiments in A549 and RAW264.7 cells, respectively. Then A549 and RAW264.7 cells were infected with IAV-H1N1/FM1 and HCoV-OC43 viruses respectively, followed by treatment with TBM II. Immunofluorescence analysis revealed that PACT-knockdown cells exhibited enhanced production of the inflammatory cytokines IL-6 and IFN-γ, alongside a reduced capacity of TBM II to suppress their expression (Fig. 8A and Supporting Information Fig. S8B). Notably, PACT knockdown also increased the viral load while impairing the antiviral potency of TBM II (Fig. 8B), which collectively suggests that TBM II modulates both the inflammatory response and viral replication in a PACT-dependent manner. We further assessed cytopathic changes of TBM II after PACT knockdown and PACT overexpression. PACT knockdown led to pronounced cell death and detachment, which was markedly attenuated by TBM II (Fig. 8C). By contrast, PACT-overexpressing cells showed no obvious damage, and TBM II further bolstered cellular protection under these conditions (Fig. S8C). Concurrently, Cells were harvested at sequential time points (0−48 h) following infection with IAV-H1N1/FM1 or HCoV-OC43 to profile the expression dynamics of RIG-I-associated proteins. Consistent with earlier observations in lung tissue, both viruses triggered a transient up-regulation of PACT, RIG-I and IFN-β, after which their levels declined (Figs. 8D and E). Nevertheless, viral load persisted at high levels during the entire downturn of these immune markers (Fig. S8A). Furthermore, we demonstrated that TBM II effectively rescues the reduced Rigi expression observed in virus-infected cells following PACT knockdown (Fig. S8F). We next assessed alterations in the RIG-I signaling cascade, finding that infected PACT-knockdown cells displayed a broad suppression of the pathway, as evidenced by concurrently diminished levels of RIG-I, MAVS, and IFN-β proteins as well as reduced IRF-3 phosphorylation, all of which were reversed upon TBM II administration. Conversely, in infected cells overexpressing PACT, TBM II elicited a significantly stronger induction of these same signaling components, thereby also potentiating IFN-β expression to a greater extent (Figs. 8F, G and Figs. S8D and E). Taken together, these results demonstrated that PACT as the critical determinant of TBM II's antiviral effect, allowing it to boost host immunity during the late phase of infection by activating the RIG-I pathway and increasing IFN-β secretion, thereby helping to overcome the virus's suppression of innate immunity during this period. Furthermore, while TBM II specifically upregulates IFN-β expression during viral infection, it does not alter its steady-state expression in uninfected cells, suggesting that it does not perturb the innate immune homeostasis of normal cells (Fig. S8G).

2.9. The RIG-I pathway is a critical pathway for the antiviral efficacy of TBM II via targeting PACT

To determine whether the antiviral activity of TBM II is dependent on the RIG-I pathway, we employed CRISPR/Cas9 gene editing to target its key components—RIG-I, MAVS, and IFN-β—in A549 cells, thereby establishing three corresponding isogenic knockout cell lines (Fig. 9A). After confirming by PCR, Sanger sequencing, and Western blot that the target genes were completely knocked out in A549 cells (Figs. 9B and C, and Supporting Information Fig. S9), we infected all three cell lines with IAV-H1N1/FM1 and subsequently administered TBM II. At 48 h post-treatment, we observed that cells with knockout of RIG-I, MAVS, or IFN-β harbored a higher viral load than wild-type cells. Moreover, the efficacy of TBM II in reducing the viral load was substantially attenuated, to the point of being largely ineffective, in these knockout cell lines (Fig. 9D). These findings indicate that the antiviral effect of TBMII in lowering viral load is dependent on the RIG-I signaling pathway. It is noteworthy that in cells deficient for RIG-I, MAVS, or IFN-β, TBM II exhibited a markedly diminished capacity to upregulate IFN-β (Fig. 9E). As a pivotal type I interferon, IFN-β plays a central role in immune potentiation and antiviral responses; thus, this impairment implies that TBM II requires a functional upstream signaling axis to exert its antiviral effect. Supporting this at the protein level, Western blot results showed that TBM II could not elevate IFN-β protein expression in RIG-I-, MAVS-, or IFN-β-knockout cells, in stark contrast to its effect in wild-type cells (Fig. 9F). Taken together, our findings support the conclusion that the broad-spectrum antiviral activity of TBM II is mediated through the targeting of

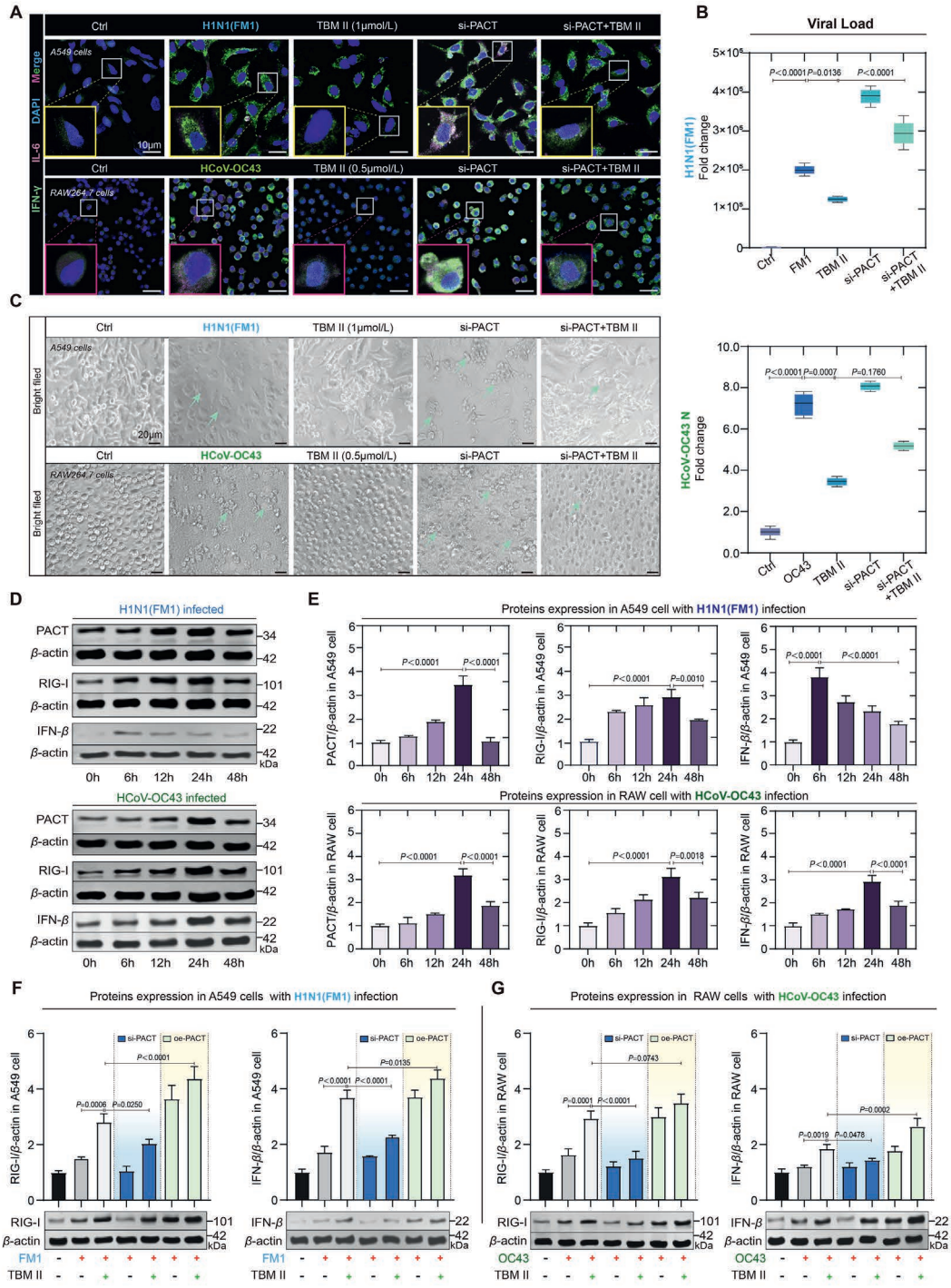

Figure 8 The knockdown or overexpression of the PACT gene influences the antiviral efficacy of TBM II *in vitro*. (A) Confocal microscopy evaluated IFN-γ and IL-6 expression under conditions of PACT knockdown, viral infection, and TBM II treatment. (B) RT-qPCR was employed to determine the viral load of two viruses following PACT knockdown and subsequent treatment with TBM II ($n=3$). (C) Concurrently, bright-field microscopy assessed cellular morphology following identical experimental perturbations (Cytopathic death is indicated by green arrows). (D, E) Westen blot analysis of PACT, RIG-I, and IFN-β in cells at 48 h post-infection with the two viruses ($n=3$). (F, G) Western blot analysis of TBM II-mediated modulation of RIG-I and IFN-β protein expression following PACT knockdown or overexpression and subsequent two-viral infection ($n=3$). Scale bar = 10 um/20 um, data present as mean ± SD. All experimental groups, except the Ctrl group, were infected with the virus.

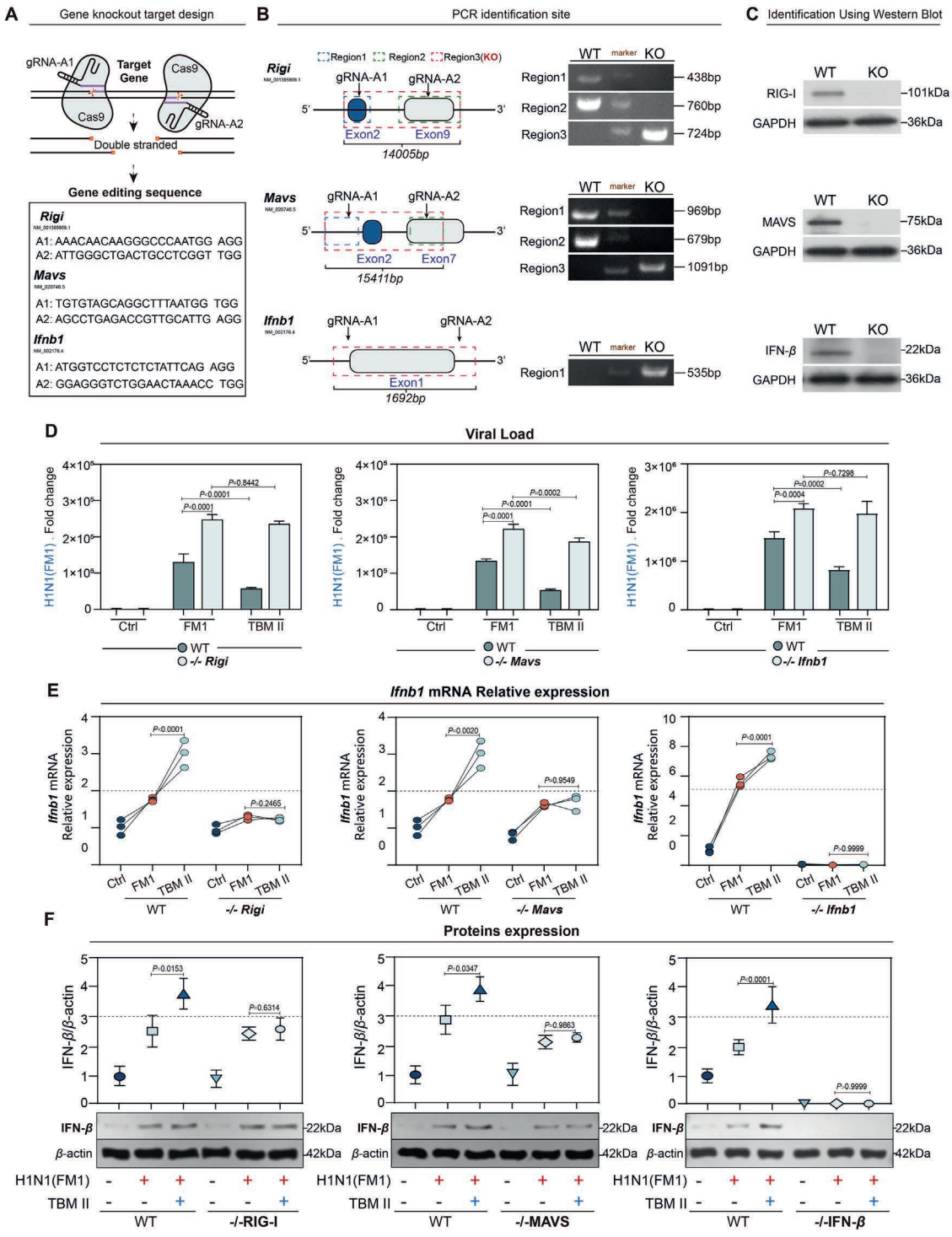

Figure 9 Impact of knockout of key RIG-I signaling pathway genes on the antiviral efficacy of TBM II. (A) Schematic of the target sites for generating knockouts of RIG-I, MAVS, and IFN-β. (B) Genotyping PCR confirms the targeted loci for the three gene knockouts. (C) Verification of successful gene knockout by Western blot analysis. (D) Effect of TBM II on viral load post-infection in gene-knockout cells ($n=3$). (E) Expression level of *Ifnb1*mRNA determined by RT-qPCR ($n=3$). (F) Western blot detection of IFN-β protein levels in gene-knockout cells upon TBM II treatment ($n=3$). All experimental groups, except the Ctrl group, were infected with the virus.

PACT, resulting in RIG-I pathway activation and potentiation of IFN-β production and innate immunity.

3. Discussion

PACT, as a host target, has demonstrated considerable potential in antiviral research. Its dual mechanisms of activating the host's innate immune response and directly inhibiting viral replication render it a promising broad-spectrum antiviral target[28]. In recent years, "target−ligand compounds" have achieved significant advancements in the treatment of viral diseases. These compounds, by precisely binding to specific biomolecules, can modulate key signaling pathways or functions, thereby achieving highly efficient and specific therapeutic effects[29]. For instance, Paxlovid, an inhibitor targeting Mpro of SARS-CoV-2, has been successfully marketed for the treatment of COVID-19[30]. Moreover, drug design strategies based on target structure, such as multi-site occupancy and allosteric targeting, have provided new approaches to overcoming drug resistance[31]. However, antiviral drug research targeting host factors remains relatively underexplored. Our study has established that the ligand compound TBM II, identified through targeting PACT, possesses antiviral efficacy both *in vitro* and *in vivo*. It effectively reduces the viral load of SARS-CoV-2, HCoV-OC43, and IAV-H1N1 (FM1) virus. And TBM II also alleviated cellular and pulmonary inflammatory responses elicited by viral infection and diminishes the expression of pro-inflammatory factors TNF-α, IL-1β, IL-6, and IFN-γ (Figs. 1, 3 and 4). These findings highlight the reliability and effectiveness of our screening strategy. In addition, the development of broad-spectrum antiviral drugs against respiratory viruses is of utmost urgency. Such drugs not only effectively combat multiple pathogens but also reduce the risk of drug resistance[32]. Traditional Chinese medicine (TCM) compounds, with their broad-spectrum properties, have shown great potential in fighting various viral infections. Studies have demonstrated that numerous TCM herbs and their extracts are rich in bioactive components that can directly inhibit viral replication or modulate the host immune response. The microRNA MIR2911 from *honeysuckle* effectively inhibits multiple influenza subtypes, including H1N1[33]. *Cepharanthine* and its analogs have been identified as broad-spectrum coronavirus inhibitors[34]. Therefore, in our drug screening, we restricted the ligand compounds to those derived from traditional Chinese medicine (TCM). By integrating TCM compounds with host targets, we aimed to enhance the potential broad-spectrum antiviral capabilities of the drugs. Target Protein Fishing Assay, CETSA, DARTS, SPR, and MST assays confirmed that TBM II not only specifically binds to PACT but also exhibits excellent binding affinity and stability. The potential binding site is located at Thr78 of PACT, which strongly corroborates our previous virtual and high-throughput screenings (Fig. 2).

TBM II, a triterpenoid saponin compound derived from the traditional Chinese medicine Rhizoma Bolbostematis, has garnered attention for its potential antiviral properties[35]. Researchers have discovered that the saponins from Rhizoma Bolbostematis can specifically bind to the host protein NPC1 in late endosomes, thereby blocking the membrane fusion between the envelope glycoproteins of SARS-CoV-2 and Ebola virus with NPC1, which in turn inhibits viral replication[24]. This represents an emerging area of research where drugs target host factors to exert antiviral effects, with TBM II showing *in vitro* inhibitory activity against SARS-CoV-2. However, the study did not involve *in vivo* antiviral experiments. Viruses typically activate the RIG-I/MAVS/IRF3 pathway to induce IFN-β production in response to infection. However, as viruses replicate and proliferate, they may employ various strategies to evade, suppress, or reprogram the host immune system, thereby inhibiting signaling pathways or negatively regulating IFN-β gene expression to weaken the host's antiviral response and increase disease progression risk. Studies showd that viral proteins suppress interferon responses through distinct mechanisms: influenza PA blocks IRF3 activation[27], SARS-CoV/SARS-CoV-2 NSP5 traps phosphorylated IRF3 in the cytoplasm[36], MERS-CoV nucleocapsid disrupts TRIM25-mediated RIG-I ubiquitination[37], and BCoV N inhibits MDA5/MAVS/TBK1 signaling[38]. Although these viruses initially activate interferon pathways, later-stage suppression becomes dominant. Viral evolution may amplify this immunosuppression, increasing disease risks. Dynamic profiling of the two viruses in our study reproduced the same pattern: infection transiently activates the RIG-I pathway and promotes IFN-β secretion, followed by a subsequent decline (Fig. 7A and B and 8D, E, Figs. S7A and S8A). Therefore, maintaining or enhancing IFN-β levels through pharmacological intervention represents an important antiviral strategy. Our work used intranasal administration to infect mice with HCoV-OC43 and IAV-H1N1 (FM1) viruses (Fig. 3A). We observed a decrease in $CD4^+$ and $CD8^+$ T lymphocytes in the blood of infected mice, which was reversed upon treatment with TBM II (Fig. 3E−H). Moreover, TBM II significantly increased the expression of IFN-β (Fig. 7E−H). These findings suggest that TBM II has immunomodulatory effects, enhancing the body's defense against pathogens. Thus, we hypothesized that TBM II may exert its antiviral effects through immunomodulation. The RIG-I signaling pathway, associated with PACT, is a canonical immune regulatory pathway. RIG-I, a key member of the RIG-I-like receptors (RLRs) family, recognizes viral dsRNA in the cytoplasm to activate antiviral immune responses[39]. RIG-I primarily identifies short dsRNA with 5′-phosphate groups. The receptor interacts with the adaptor protein MAVS *via* its N-terminal CARD domain, activating downstream signaling pathways and phosphorylating IRF3 or IRF7 transcription factors, which promote the expression of IFN-I (IFNα and IFNβ) and other antiviral genes[40]. Therefore, we proposed that TBM II may positively regulate the RIG-I signaling pathway by targeting PACT, thereby promoting IFN-I secretion to exert antiviral effects. However, there is currently no antiviral drug research targeting the PACT-RIG-I pathway.

Single-cell sequencing was utilized to profile signaling pathways and gene expression in murine lung tissues, revealing significant expression differences in the RIG-I signaling pathway and its associated genes following viral infection and drug intervention. The results indicated that TBM II up-regulated the expression of PACT, RIG-I, MAVS, and IRF-3 genes, with this effect being most pronounced in macrophages (Fig. 6D and Fig. S6D). Subsequent validation using immunofluorescence, Western blot, and q RT-PCR corroborated these findings (Figs. 7E−H). As previously reported, PACT can physically bind to the C-terminal repressor domain (CTD) of RIG-I[13]. Consistent with these reports, we further confirmed that TBM II promotes the binding of PACT to RIG-I, with the binding sites located in the CTD domain of RIG-I and the 1-103 fragment of PACT protein (Figs. 6E−G and Fig. S6C). We have also demonstrated in Section 2.2 that PACT is a highly stable target of TBM II (Fig. 2 and Fig. S2). This binding is crucial for RIG-I activation, as it relieves the auto-inhibition of RIG-I, allowing it to recognize viral RNA and

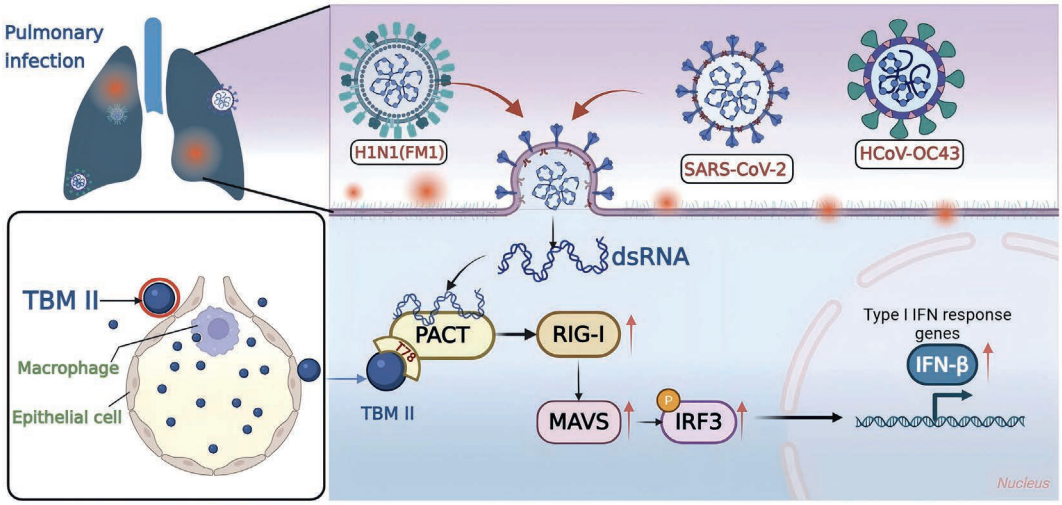

Figure 10 TBM II selectively binds to PACT and promotes the PACT-RIG-I interaction. This initiates the RIG-I signaling cascade. Such molecular events upregulate type I interferon (IFN-I) production, enhance the innate immune response, and consequently achieve broad-spectrum antiviral efficacy.

initiate downstream antiviral signaling pathways, thereby activating IFN-I production. We therefore performed PACT-knockdown and overexpression in cells prior to viral infection and TBM II treatment. Following PACT-knockdown, enhanced HCoV-OC43 and IAV-H1N1 (FM1) infection was observed, with diminished therapeutic efficacy of TBM II evidenced by reduced IFN-β up-regulation and increased pro-inflammatory cytokine expression. To determine whether the antiviral activity of TBM II involves the PACT-mediated RIG-I pathway, we performed Western blot analysis. The results showed that PACT-knockdown impaired the ability of TBM II to enhance the expression of RIG-I/MAVS and the phosphorylation of IRF-3 in infected cells. Conversely, PACT overexpression amplified TBM II-induced up-regulation of these proteins. Moreover, we generated knockout cell lines targeting key components of this signaling cascade: RIG-I, MAVS, and IFN-β. Following infection with IAV-H1N1 (FM1), cells deficient in these genes exhibited significantly higher viral loads compared to wild-type controls. Moreover, the potent therapeutic effect of TBM II was markedly attenuated or completely abolished in these knockout cells (Fig. 9). These results collectively demonstrate that TBM II exerts its antiviral action by targeting PACT to activate the RIG-I signaling pathway, thereby enhancing IFN-β production and boosting innate immune responses. These observations are fully consistent with our initial scientific hypothesis (Fig. 10).

4. Conclusions

In summary, "target−ligand compounds" represent an innovative approach for the development of broad-spectrum antiviral drugs, and the PACT target undoubtedly holds great potential for application. This represents the first reported ligand discovery targeting PACT to date. Beyond TBM II, additional traditional Chinese medicine compounds identified in the preliminary screening phase of this study may similarly exert antiviral effects *via* PACT, warranting further investigation in our subsequent research. Moreover, investigations into the mechanisms downstream of PACT are not confined to the RIG-I signaling pathway but can also be extended to other avenues [41−43]. Although the antiviral mechanisms of different drugs *via* PACT are diverse, the ultimate goal remains consistent: to expand our pharmacological arsenal for future responses to emerging viral pandemics.

5. Experimental

5.1. Drug and reagents

Tubeimoside II was obtained from Target Mol Co., Ltd. (Boston, USA). Recombinant Human PACT His Protein was sourced from Novus Biologicals Co., Ltd. (MA, USA). The PROCARTAPLEX 6 PLEX kit for detecting inflammatory cytokines and Lipofectamine® 3000 were purchased from Thermo Fisher Co., Ltd. (Waltham, MA, USA).

5.2. Animals

BALB/c mice (body weight 13−15 g) were obtained from Vital River Laboratory Animal Technology Co., Ltd. (Beijing, China), and ICR mice of similar weight were sourced from Sibeifu Biotechnology Co., Ltd. (Beijing, China). All animal were approved by the Animal Welfare Ethics Committee of the China Academy of Chinese Medical Sciences (Approval Nos: 2024D027, 2024D030).

5.3. Virtual screening

The fishing database encompasses a range of chemical libraries such as Targetmol, Chemdiv, Specs, IBS, HTS Biochemie Innovationen, Princeton, Vitas-M, Alinda, Enamine, Bionet, Otava, Asinex, UkrOrg Synthesis, IB Screen, and Life chemicals. Molecular docking commences with uploading the target protein structure in Protein Data Bank format followed by structural validation. The docking box position and size defining the binding site search space are specified either through selection of the target amino acid sequence or by defining spatial coordinates and box dimensions. After confirming the protein ligand and docking box

users configure the scoring function such as Vina Vinardo or AutoDock4 select a search mode categorized as Fast Balanced or Detailed determine the number of output poses and set ligand conformational sampling options.

5.4. Plasmid construction

Primers with restriction enzyme sites at both ends were designed based on the coding sequence (CDS) region of Homo sapiens PACT (Gene Bank accession number NM_003690.5) retrieved from the NCBI GenBank database. The human PACT siRNA hPACT (PRKRA)-502 (Catalog No. R16589) was synthesized by Sangon Biotech (Shanghai) Co., Ltd. The human PACT overexpression plasmid pHG-CMV-PRKRA-mEGFP (Catalog No. HG-HO00369) was purchased from Honor Gene (Changsha, China).

5.5. Cell cultures

Caco-2-N, RAW264.7, and A549 cell lines were cultured in DMEM (Gibco, China) supplemented with 10% FBS and 50 IU/mL penicillin-streptomycin under standard conditions (37 °C, 5% CO_2). Mycoplasma-free status was confirmed through routine screening. Cells were seeded in 96-well plates at 2×10^4 cells/well and allowed to adhere for 12 h before exposure to gradient concentrations of the test compound (Caco-2-N cells provided by Dr. Qiang Ding from Tsinghua University).

5.6. Generation of SARS-CoV-2 trVLP

RT-qPCR-amplified target fragments were enzymatically digested, purified, and ligated *via* T4 ligase. The cDNA construct was phenol-chloroform extracted, isopropanol-precipitated, and reconstituted in 10 μL nuclease-free H_2O. For recombinant virus generation, in vitro-transcribed RNA was electroporated into Caco-2-N cells (8×10^6 cells/0.4 mL Opti-MEM) using 270 V/950 μF parameters (Bio-Rad Gene Pulser). GFP expression was monitored at 17 h post-transfection. P0 virus harvested at 72 h was amplified in fresh Caco-2-N cultures. Clarified supernatant was filtered (0.45 μmol/L), aliquoted, and cryopreserved (−80 °C). Reagent requests should be addressed to Dr. Qiang Ding (qding@tsinghua.edu.cn)[44].

5.7. High-content imaging (HCI) systems are utilized for the analysis of the virulence of the SARS-CoV-2 trVLP

Caco-2-N cells were seeded in black-wall 96-well plates at 3×10^4 cells/well with experimental groups configured as: Control, infection model, positive drug and TCM compounds. At 70%−80% confluency, cultures underwent synchronized virological challenge with SARS-CoV-2 GFP/ΔN VLPs under standard culture conditions (37 °C, 5% CO_2) for 12 h, with intervention timing calibrated to pre-GFP signal manifestation. Following this, the individual drugs at various dosages were administered and the cells were further incubated for 48 h under the same conditions. The expression of the virus post-treatment (GFP signal) was then assessed using a high-content imaging system, Image Xpress® Micro XLS, to determine whether the administered drugs possess antiviral activity against SARS-CoV-2 virus.

5.8. Target protein fishing assay

WED-conjugated epoxy-activated Sepharose 6B matrices (GE Healthcare) were prepared following standardized coupling procedures. Cellular lysates underwent affinity binding with WED-immobilized matrices or free WED through 12-h cold incubation (4 °C), followed by three sequential PBS washes to eliminate non-specifically adsorbed proteins. Captured protein complexes were subsequently characterized through argentometric detection, immunoblotting analysis, and liquid chromatography−tandem mass spectrometry.

5.9. CETSA experiment to verify drug affinity for PACT

After drug treatment, cells were subjected to thermal denaturation across a gradient of 37−68 °C, followed by lysis in RIPA buffer supplemented with protease inhibitors. Insoluble aggregates were removed by high-speed centrifugation (16,000×*g*, 15 min) or 0.22 μmol/L filtration, with concurrent collection of both the precipitated and soluble protein fractions. The soluble proteins were then separated by SDS-PAGE (12% gel, 120 V) and transferred to PVDF membranes using a semi-dry method. PACT protein was detected with validated primary antibodies (1:1000 dilution) and horseradish peroxidase-conjugated secondary antibodies (1:5000), with visualization achieved through chemiluminescent detection.

5.10. SPR analysis

The binding assay was conducted on a BIAcore T200 (25 °C) with CM5 chips. After EDC/NHS activation (200/50 μmol/L, 10 μL/min, 420 s), target protein PACT in 10 mmol/L sodium acetate was dual-immobilized (50 μL, 10 μL/min, 420 s). Ethanolamine (1 mol/L, 10 μL/min) blocked residual sites. PBS (pH 5.0) served as reference. Analyte dilutions (PBS) were injected (10 μL/min, 150 s) with intermittent regeneration (10 mmol/L glycine-HCl, pH 2.0). Reference-subtracted sensorgrams were processed *via* 1:1 Langmuir global fitting (BIAcore Evaluation v2.0) for kinetic analysis, with data visualization using Origin 7.

5.11. Drug affinity responsive target stability assay (DARTS)

HEK293T cells in the logarithmic growth phase were harvested from culture dishes, and total protein was extracted. The proteins were lysed and the supernatant was collected following centrifugation. The lysate was then divided equally into five groups, to which different concentrations of TBM II solution (0.25, 0.5, and 1 μmol/L) were added. The control group received an equivalent volume of DMSO. After mixing at room temperature for 2 h, followed by incubation at 37 °C for 10 min. The samples were centrifuged (20,000×*g*, 20 min, 4 °C) and the resultant supernatant was combined with 5 × loading buffer followed by thermal denaturation (100 °C, 10 min). Protein preparations were electrophoretically resolved for immunoblotting detection.

5.12. Microscale thermophoresis (MST) assay

Fluorescent labeling of PACT was performed using the Monolith NT protein conjugation system. A concentration gradient of TBM II was serially diluted and incubated with the tagged protein. Capillary-based thermophoretic migration was monitored through the Monolith NT.115 platform (NanoTemper Technologies,

Munich, Germany) following sample loading. Binding kinetics were quantified using the manufacturer's proprietary analysis suite.

5.13. Western blot assay

Western blot analysis was carried out on samples from both *in vivo* and *in vitro* experiments. Protein concentrations were quantified using a BCA protein assay kit (Biorigin, Beijing, China). Proteins (10% SDS-PAGE/PVDF) were FBS-blocked and immunoprobed (4 °C/overnight): β-actin (1:10,000, Proteintech, Chicago, IL, USA), PACT (1:1500, Proteintech, Chicago, IL, USA), RIG-1 (1:3000, Proteintech, Chicago, IL, USA), MAVS (1:9000, Proteintech, Chicago, IL, USA), IRF3 (1:5000, Proteintech, Chicago, IL, USA), Phospho-IRF3 (1:2000, Proteintech, Chicago, IL, USA) and IFN-β (1:500, Proteintech, Chicago, IL, USA). The membranes were incubated with goat anti-rabbit IgG(H + L) (1:8000, Proteintech, Chicago, IL, USA) for 1 h at room temperature. Signals were captured and analyzed *via* ImageJ.

5.14. RT-qPCR assay

The mRNA levels of RIG-I pathway-related genes were quantified by RT-qPCR. Total RNA was isolated from lung tissues and cultured cells with TRIzol reagent (Life Technologies, USA), followed by RT-qPCR analysis using Evo M-MLV One Step RT-qPCR Kit (ACCURATE BIOTECHNOLOGY(HUNAN) CO., LTD, ChangSha, China). Primer sequences are provided in Supporting Information Table S2.

5.15. Establishment, grouping, and medication administration in animal models

A total of 60 ICR and Balb/c mice were selected, with an equal number of males and females, and randomly assigned to six different groups based on their body weight to establish models for IAV-H1N1/FM1 and HCoV-OC43 virus infection. The groups were categorized as follows: normal control group, model control group, Oseltamivir/Azvudine control group, and three dosage groups of TBMII (2.6, 1.3, and 0.65 mg/kg), The positive drug doses were FNC (2.0 mg/kg) and OSV (27.5 mg/kg). Under mild anesthesia with isoflurane, all groups except the normal control group were infected *via* the intranasal route with 15 $TCID_{50}$ of the IAV-H1N1/FM1 and HCoV-OC43 virus. The normal control group received a physiological saline solution, with each mouse receiving 35 μL of the intranasal solution. On the day of infection, mice in each treatment group were administered medication *via* gavage, with a dosage volume of 0.2 mL/10 g, once daily for five consecutive days. The IAV-H1N1/FM1 and HCoV-OC43 virus were purchased from the American Type Culture Collection (ATCC), propagated in our laboratory, and stored at −80 °C.

5.16. H&E staining for histopathological evaluation of murine lung tissue alterations

Pulmonary specimens underwent immersion-fixation in 10% neutral buffered formalin followed by progressive ethanol dehydration. Subsequent to alcohol treatment, xylene-mediated clearing preceded final encapsulation in histological-grade paraffin wax. Sections of the embedded tissues, approximately 5 ± 1 μmol/L in thickness, were cut using a microtome, floated onto glass slides, and allowed to dry in a temperature-controlled chamber. Subsequently, H&E-stained slides revealed morphology. The presence of any pathological alterations in the murine lung tissue was examined using light microscopy.

5.17. Immunofluorescence assay

Cellular/tissue specimens underwent immersion-fixation in 4% paraformaldehyde (PFA), followed by 0.4% Triton X-100 permeabilization treatment and 1-h nonspecific site blocking with 5% BSA under room temperature equilibration. Immunostaining employed species-matched primary immunoprobes targeting PACT, RIG-I, IRF3, IFN-γ, and IL-6 (monoclonal/polyclonal sources) through 12−16 h cold-phase incubation (4 °C), succeeded by 60 min exposure to fluorochrome-conjugated secondary antibodies under light-protected ambient conditions. Chromatin visualization utilized DAPI nuclear counterstaining (10-min protocol). High-resolution imaging was performed on a Leica SP5 laser-scanning confocal microscopy system (63 × oil objective), with subsequent digital quantification of fluorescence signals *via* ImageJ threshold-based detection module for spatial protein profiling.

5.18. Generation of knockout cell lines

CRISPR-Cas9-mediated knockout of the RIGI, MAVS, and IFNB1 genes was performed using commercially available ribonucleoprotein (RNP) complexes. Targeted knockout of RIGI, MAVS, and IFNB1 was performed using two sgRNAs per gene designed *via* http://crispr.mit.edu: RIGI (AAACAACAAGGGCCCAATGG AGG, ATTGGGCTGACTGCCTCGGT TGG), MAVS (TGT GTAGCAGGCTTTAATGG TGG, AGCCTGAGACCGTTGCATTG AGG), and IFNB1 (ATGGTCCTCTCTCTATTCAG AGG, GGAGGGTCTGGAACTAAACC TGG). These were delivered as plasmids or RNP complexes *via* electroporation (Neon System). Single-cell clones were isolated, screened by PCR and Sanger sequencing for biallelic indels, and isogenic lines (*e.g.,* +/+, −/−) were established and maintained under standard conditions.

5.19. Statistical analysis

Statistical analyses were executed through GraphPad Prism 10.2.3. Intergroup comparisons were conducted *via* One-way ANOVA, with $P < 0.05$ indicating statistical significance.

Acknowledgements

This study was supported by Scientific and Technological Innovation Project of China Academy of Chinese Medical Sciences (No. CI2026A04601, CI2024E003, China); National Science and Technology Major Project (No. 2024ZD0528801, China); National Administration of Traditional Chinese Medicine (No. ZYYCXTD-D-202406, China); Natural Science Foundation of Beijing Municipality (No. 7252250, L222130, China).

Author contributions

Xian Liu drafted the manuscript with contribution from all authors. Shanshan Guo supervised the whole project. Xian Liu, Dan Xie, Mengyao Cui and Chengpeng Sun revised and reviewed the manuscript. Xian Liu, Mengyao Cui and Xiaowei Yang constructed the experimental silicosis model. Xian Liu, Xiaowei

Yang, and Yu Zhang contributed to harvesting animals and lung functional test. Ronghua Zhao and Shuangrong Gao performed all the pathological experiments. Xian Liu analyzed the single-cell RNA sequencing data. All authors analyzed the other data. We thank Professor Ding (Tsinghua University, Beijing, China) for generously providing the SARS-CoV-2 trVLP and Caco-2-N cells. All authors approved of the final version of the manuscript and are accountable for all aspects of this work.

Conflicts of interest

The authors declare that there are no conflicts of interest.

Data availability statement

Experimental datasets are incorporated within the manuscript and Supporting Information files, with primary data supporting all findings. Single-cell transcriptomic profiles have been deposited in the Gene Expression Omnibus (GEO) repository under accession code GSE292752.

Appendix A. Supporting information

Supporting information to this article can be found online at https://doi.org/10.1016/j.apsb.2026.03.020.

References

1. Husain M. Influenza A virus and acetylation: the picture is becoming clearer. *Viruses* 2024;**16**:131.
2. Carabelli AM, Peacock TP, Thorne LG, Harvey WT, Hughes J, Peacock SJ, et al. SARS-CoV-2 variant biology: immune escape, transmission and fitness. *Nat Rev Microbiol* 2023;**21**:162−77.
3. Luong QXT, Hoang PT, Ho PT, Ayun RQ, Lee TK, Lee S. Potential broad-spectrum antiviral agents: a key arsenal against newly emerging and reemerging respiratory RNA viruses. *Int J Mol Sci* 2025;**26**:1481.
4. Shin WJ, Seong BL. Novel antiviral drug discovery strategies to tackle drug-resistant mutants of influenza virus strains. *Expert Opin Drug Discov* 2019;**14**:153−68.
5. Zheng Y, Li S, Song K, Ye J, Li W, Zhong Y, et al. A broad antiviral strategy: inhibitors of human DHODH pave the way for host-targeting antivirals against emerging and re-emerging viruses. *Viruses* 2022;**14**: 928.
6. Zhang Y, Gao H, Hu X, Wang Q, Zhong F, Zhou X, et al. Structure-based discovery and structural basis of a novel broad-spectrum natural product against the main protease of coronavirus. *J Virol* 2022;**96**: e0125321.
7. Kumari M, Lu R-M, Li M-C, Huang J-L, Hsu F-F, Ko S-H, et al. A critical overview of current progress for COVID-19: development of vaccines, antiviral drugs, and therapeutic antibodies. *J Biomed Sci* 2022;**29**:68.
8. Zhang Y, Chen S, Tian Y, Fu X. Host factors of SARS-CoV-2 in infection, pathogenesis, and long-term effects. *Front Cell Infect Microbiol* 2024;**14**:1407261.
9. Li S, Peters GA, Ding K, Zhang X, Qin J, Sen GC. Molecular basis for PKR activation by PACT or dsRNA. *Proc Natl Acad Sci U S A* 2006; **103**:10005−10.
10. Dabo S, Maillard P, Collados Rodriguez M, Hansen MD, Mazouz S, Bigot DJ, et al. Inhibition of the inflammatory response to stress by targeting interaction between PKR and its cellular activator PACT. *Sci Rep* 2017;**7**:16129.
11. Chukwurah E, Farabaugh KT, Guan BJ, Ramakrishnan P, Hatzoglou M. A tale of two proteins: PACT and PKR and their roles in inflammation. *FEBS J* 2021;**288**:6365−91.
12. David RYS, Combredet C, Najburg V, Millot GA, Beauclair G, Schwikowski B, et al. LGP2 binds to PACT to regulate RIG-I- and MDA5-mediated antiviral responses. *Sci Signal* 2019;**12**:eaar3993.
13. Kok KH, Lui PY, Ng MH, Siu KL, Au SW, Jin DY. The double-stranded RNA-binding protein PACT functions as a cellular activator of RIG-I to facilitate innate antiviral response. *Cell Host Microbe* 2011;**9**:299−309.
14. Chen Z, Ye S-y. Research progress on antiviral constituents in traditional Chinese medicines and their mechanisms of action. *Pharm Biol* 2022;**60**:1063−76.
15. Ma LL, Liu HM, Luo CH, He YN, Wang F, Huang HZ, et al. Fever and antipyretic supported by traditional Chinese medicine: a multi-pathway regulation. *Front Pharmacol* 2021;**12**:583279.
16. Rahman MA, Ueda K, Honda T. A traditional Chinese medicine, maoto, suppresses hepatitis b virus production. *Front. Cell. Infect* 2021;**10**:581345.
17. Xu Y, Li S, Zhao R, Bao L, Geng Z, Sun Q, et al. Isorhamnetin alleviates pathological damage in influenza A virus strain PR8-induced pneumonia by activating the Nrf2/HO-1 pathway and suppressing apoptosis. *Sci Tradit Chin Med* 2025;**3**:28−39.
18. de Matos PH, da Silva TP, Mansano AB, Gancedo NC, Tonin FS, Pelloso FC, et al. Bioactive compounds as potential angiotensin-converting enzyme II inhibitors against COVID-19: a scoping review. *Inflamm Res* 2022;**71**:1489−500.
19. Zou Q, Chen Y, Qin H, Tang R, Han T, Guo Z, et al. The role and mechanism of TCM in the prevention and treatment of infectious diseases. *Front Microbiol* 2023;**14**:1286364.
20. Li BH, Li ZY, Liu MM, Tian JZ, Cui QH. Progress in traditional Chinese medicine against respiratory viruses: a review. *Front Pharmacol* 2021;**12**:743623.
21. Zhang J, Yan J, Dong H, Zhang R, Chang J, Feng Y, et al. Dimeric sesquiterpenoids with anti-inflammatory activities from Inula britannica. *Chin J Nat Med* 2025;**23**:961−71.
22. Chen Y, Zhu X, Wang K, Zou W, Zhou F. Tubeimoside II inhibits TGF-β1-induced metastatic progression of human retinoblastoma cells through suppressing redoxosome-dependent EGFR activation. *Chem Biol Interact* 2021;**335**:109367.
23. Liu WY, Zhang WD, Chen HS, Gu ZB, Li TZ, Chen WS. New triterpenoid saponins from bulbs of bolbostemma paniculatum. *Planta Med* 2004;**70**:458−64.
24. Khan I, Li S, Tao L, Wang C, Ye B, Li H, et al. Tubeimosides are pan-coronavirus and filovirus inhibitors that can block their fusion protein binding to niemann-pick C1. *Nat Commun* 2024;**15**:162.
25. Niu J, Shen L, Huang B, Ye F, Zhao L, Wang H, et al. Non-invasive bioluminescence imaging of HCoV-OC43 infection and therapy in the central nervous system of live mice. *Antiviral Res* 2020;**173**:104646.
26. Wu Y, Xu X, Chen Z, Duan J, Hashimoto K, Yang L, et al. Nervous system involvement after infection with COVID-19 and other coronaviruses. *Brain Behav Immun* 2020;**87**:18−22.
27. Yi C, Zhao Z, Wang S, Sun X, Zhang D, Sun X, et al. Influenza A virus PA antagonizes interferon-β by interacting with interferon regulatory factor 3. *Front Immunol* 2017;**8**:1051.
28. Brisse M, Ly H. Viral inhibitions of PACT-Induced RIG-I activation. *Oncotarget* 2017;**8**:60725−6.
29. Ma Y, Frutos-Beltrán E, Kang D, Pannecouque C, De Clercq E, Menéndez-Arias L, et al. Medicinal chemistry strategies for discovering antivirals effective against drug-resistant viruses. *Chem Soc Rev* 2021;**50**:4514−40.
30. Hashemian SMR, Sheida A, Taghizadieh M, Memar MY, Hamblin MR, Baghi HB, et al. Paxlovid (Nirmatrelvir/Ritonavir): a new approach to Covid-19 therapy?. *Biomed Pharmacother* 2023;**162**:114367.
31. Hao GF, Yang SG, Yang GF. Structure-based design of conformationally flexible reverse transcriptase inhibitors to combat resistant HIV. *Curr Pharm Des* 2014;**20**:725−39.
32. Maarifi G, Martin MF, Zebboudj A, Boulay A, Nouaux P, Fernandez J, et al. Identifying enhancers of innate immune signaling as broad-spectrum antivirals active against emerging viruses. *Cell Chem Biol* 2022;**29**. 1113−25.e6.

33. Zhou Z, Li X, Liu J, Dong L, Chen Q, Liu J, et al. Honeysuckle-encoded atypical microRNA2911 directly targets influenza A viruses. *Cell Res* 2015;**25**:39−49.
34. Leng L, Xu Z, Hong B, Zhao B, Tian Y, Wang C, et al. Cepharanthine analogs mining and genomes of stephania accelerate anti-coronavirus drug discovery. *Nat Commun* 2024;**15**:1537.
35. Huang H, Liang M, Xu W, Zhang C, Zhang W. Identification and quantification of three tubeimosides in rhizoma bolbostematis by high performance liquid chromatography with evaporative light scattering detection and electrospray mass spectrometric detection. *Nat Prod Commun* 2008;**3**:683−8.
36. Fung SY, Siu KL, Lin H, Yeung ML, Jin DY. SARS-CoV-2 main protease suppresses type I interferon production by preventing nuclear translocation of phosphorylated IRF3. *Int J Biol Sci* 2021;**17**: 1547−54.
37. Chang CY, Liu HM, Chang MF, Chang SC. Middle East respiratory syndrome coronavirus nucleocapsid protein suppresses type I and type III interferon induction by targeting RIG-I signaling. *J Virol* 2020;**94**: e00099-20.
38. Xiangbo Z, Zhaofang Y, Jinjing G, Zhuandi G, Suocheng W. Bovine coronavirus nucleocapsid suppresses IFN-β production by inhibiting RIG-I-like receptors pathway in host cells. *Arch Microbiol* 2022;**204**: 536.
39. Ji L, Liu Q, Wang N, Wang Y, Sun J, Yan Y. Porcine dsRNA-binding protein staufen1 facilitate dsRNA-RIG-I/MDA5 binding to activate the antiviral innate immunity response. *Vet Microbiol* 2022;**272**: 109515.
40. Schmidt A, Rothenfusser S, Hopfner KP. Sensing of viral nucleic acids by RIG-I: from translocation to translation. *Eur J Cell Biol* 2012;**91**: 78−85.
41. Singh M, Fowlkes V, Handy I, Patel CV, Patel RC. Essential role of PACT-mediated PKR activation in tunicamycin-induced apoptosis. *J Mol Biol* 2009;**385**:457−68.
42. Chen S, Yang F, Cao W, Zhang X, Liu H, Zhang K, et al. Peste des petits ruminants virus nucleocapsid protein interacts with protein kinase R-activating protein and induces stress granules to promote viral replication. *J Virol* 2023;**97**:e0171222.
43. Walsh D, Mohr I. Viral subversion of the host protein synthesis machinery. *Nat Rev Microbiol* 2011;**9**:860−75.
44. Ju X, Zhu Y, Wang Y, Li J, Zhang J, Gong M, et al. A novel cell culture system modeling the SARS-CoV-2 life cycle. *PLoS Pathog* 2021;**17**:e1009439.